

Testing Star Formation Laws in a Starburst Galaxy At Redshift 3 Resolved with ALMA

P. Sharda^{2,3,4*}, C. Federrath¹, E. da Cunha¹, A. M. Swinbank^{5,6} and S. Dye⁷

¹Research School of Astronomy and Astrophysics, The Australian National University, Canberra, ACT 2611, Australia

²Department of Physics, Birla Institute of Technology and Science, Pilani, Rajasthan 333031, India

³Department of Electrical and Electronics Engineering, Birla Institute of Technology and Science, Pilani, Rajasthan 333031, India

⁴Department of Physics and Astronomy, University of Exeter, Stoker Road, Exeter EX4 4QL, UK

⁵Institute for Computational Cosmology, Durham University, Durham DH1 3LE, UK

⁶Centre for Extragalactic Astronomy, Department of Physics, Durham University, Durham, DH1 3LE, UK

⁷School of Physics and Astronomy, University of Nottingham, University Park, Nottingham NG7 2RD, UK

Accepted 2018 March 26. Received 2018 March 26; in original form 2017 December 11

ABSTRACT

Using high-resolution (sub-kiloparsec scale) data obtained by ALMA, we analyze the star formation rate (SFR), gas content and kinematics in SDP 81, a gravitationally-lensed starburst galaxy at redshift 3. We estimate the SFR surface density (Σ_{SFR}) in the brightest clump of this galaxy to be $357_{-85}^{+135} \text{ M}_{\odot} \text{ yr}^{-1} \text{ kpc}^{-2}$, over an area of $0.07 \pm 0.02 \text{ kpc}^2$. Using the intensity-weighted velocity of CO (5-4), we measure the turbulent velocity dispersion in the plane-of-the-sky and find $\sigma_{v,\text{turb}} = 37 \pm 5 \text{ km s}^{-1}$ for the clump, in good agreement with previous estimates along the line of sight, corrected for beam smearing. Our measurements of gas surface density, freefall time and turbulent Mach number allow us to compare the theoretical SFR from various star formation models with that observed, revealing that the role of turbulence is crucial to explaining the observed SFR in this clump. While the Kennicutt Schmidt (KS) relation predicts an SFR surface density of $\Sigma_{\text{SFR,KS}} = 52 \pm 17 \text{ M}_{\odot} \text{ yr}^{-1} \text{ kpc}^{-2}$, the single-freefall model by Krumholz, Dekel and McKee (KDM) predicts $\Sigma_{\text{SFR,KDM}} = 106 \pm 37 \text{ M}_{\odot} \text{ yr}^{-1} \text{ kpc}^{-2}$. In contrast, the multi-freefall (turbulence) model by Salim, Federrath and Kewley (SFK) gives $\Sigma_{\text{SFR,SFK}} = 491_{-194}^{+139} \text{ M}_{\odot} \text{ yr}^{-1} \text{ kpc}^{-2}$. Although the SFK relation overestimates the SFR in this clump (possibly due to the negligence of magnetic fields), it provides the best prediction among the available models. Finally, we compare the star formation and gas properties of this galaxy to local star-forming regions and find that the SFK relation provides the best estimates of SFR in both local and high-redshift galaxies.

Key words: Stars: formation – Submillimetre: galaxies – Galaxy: evolution – Galaxy: kinematics and dynamics – Turbulence

1 INTRODUCTION

Numerous star formation relations have been proposed in a quest to universalize the theory of star formation, by linking the star formation rate (SFR) with the mass of gas, its freefall time, virial parameter, magnetic field strength and turbulence (Silk 1997; Kennicutt 1998a; Elmegreen 2002; Shi et al. 2011; Krumholz et al. 2012 (hereafter, KDM12); Renaud et al. 2012; Escala 2015; Elmegreen & Hunter 2015; Salim et al. 2015 (hereafter, SFK15); Elmegreen 2015; Nguyen-Luong et al. 2016; Miettinen et al. 2017). While

these relations have been shown to be valid for star-forming regions in the Milky Way and local galaxies (Bigiel et al. 2008), the lack of spatial resolution has limited us in testing them on high-redshift sources with $z > 1$. Thanks to the high spatial resolution of ALMA, several high-redshift galaxies emitting in the submillimeter (sub-mm) regime have been detected and resolved over the last few years (Decarli et al. 2016; Spilker et al. 2016; Lu et al. 2017; Danielson et al. 2017; Brisbin et al. 2017), particularly if they are gravitationally-lensed by a foreground source (Smail et al. 1997, 2002; Hezaveh et al. 2013; Johnson et al. 2017; Bradač et al. 2017; Laporte et al. 2017; Wong et al. 2017; Fudamoto et al. 2017). These galaxies are known to be rigorous sites of dusty star

* E-mail: f2013440@pilani.bits-pilani.ac.in (PS)

formation where molecular gas plays a key role in modifying the structure of clusters where star formation occurs. Tracing molecular gas in these regions can give us valuable insight on the star formation characteristics of these galaxies since it is now known that molecular gas has a strong correlation with SFR whereas atomic gas does not (Wong & Blitz 2002; Bigiel et al. 2008; Blanc et al. 2009).

J090311.6+003906 (hereafter, referred to as SDP 81) was detected as a lensed galaxy in the $H - ATLAS$ survey of bright submillimeter galaxies (SMGs) by Negrello et al. (2010) where the redshift was measured as $z = 3.042 \pm 0.001$ through ground based CO measurements. It falls in the popular definition of SMGs where the $850 \mu\text{m}$ flux density $S_{850} > 3 \text{ mJy}$ and infrared luminosity $L_{\text{IR}} \gtrsim 10^{12} L_{\odot}$ (Kovács et al. 2006; Coppin et al. 2008; Hayward et al. 2011). SDP 81 has also been established to be a dusty star-forming galaxy in previous works (Negrello et al. 2014; Swinbank et al. 2015 (hereafter, S15); Dye et al. 2015; Hatsukade et al. 2015; Rybak et al. 2015a,b; Tamura et al. 2015; Wong et al. 2015; Hezaveh et al. 2016; Inoue et al. 2016). Even though there are significant uncertainties in determining the stellar mass of SDP 81, we note that it lies 1-2 orders of magnitude above the main sequence on the stellar mass – star formation rate ($M_{\star} - \text{SFR}$) plane (Speagle et al. 2014; Schreiber et al. 2015; Chang et al. 2015; Guo et al. 2015). Thus, SDP 81 falls under the category of extreme starburst galaxies and is an ideal candidate to test star formation relations. This is further confirmed by the position of SDP 81 on the star formation rate – gas mass ($\text{SFR} - M_{\text{gas}}$) plane (Sargent et al. 2014).

Our goal in this work is to extract the SFR in individual *clumps* of this galaxy and compare it with that predicted by existing star formation relations. We refer to clumps as giant star-forming regions (Genzel et al. 2006; Elmegreen et al. 2009; Bournaud et al. 2014) substantially more massive and star-forming than typical molecular clouds in the Milky Way (Cowie et al. 1995; Van den Bergh et al. 1996; Shapiro et al. 2010), and possibly showing high star formation efficiencies (Freundlich et al. 2013; Zanella et al. 2015; Cibinel et al. 2017). The paper is organized as follows: in Section 2, we summarize data reduction through lens modeling to create source plane reconstructed images (Dye et al. 2015). This section also identifies different clumps in this galaxy extracted by S15. Section 3 follows the dust spectral energy distribution (SED) fitting of a modified blackbody (MBB) and estimation of SFR surface density in the galaxy. We describe the kinematic analysis of CO (5-4) used to estimate the Mach number in Section 4. In Section 5, we present our estimates of the local gas mass and freefall time in the galaxy. Finally, we put all these parameters together to test various star formation relations and compare with the SFR surface density deduced through dust SED fitting in Section 6. We summarize our findings in Section 7.

We adopt the ΛCDM cosmology with $H_0 = 72 \text{ km s}^{-1} \text{ Mpc}^{-1}$, $\Omega_m = 0.27$, $\Omega_{\Lambda} = 1 - \Omega_m$ and a Chabrier IMF (Chabrier 2003). The luminosity distance and scale length corresponding to these parameters is 25.9 Gpc and $7.69 \text{ kpc arcsec}^{-1}$, respectively, for $z \approx 3.042$ (Wright 2006).

2 DATA REDUCTION AND ANALYSIS

ALMA observations of SDP 81 (RA = $09^{\text{h}}03^{\text{m}}11.57^{\text{s}}$, Dec = $+00^{\circ}39'06.6''$) were taken during Science Verification cycle in October 2014. In the calibrated data¹, the lensed galaxy is seen in the form of an Einstein ring, with two arcs on the eastern and western sides (Dye et al. 2014; ALMA Partnership et al. 2015). Through uv tapering, a resolution of $\sim 150 \times 120 \text{ mas}$ was achieved in the three bands (see Tables 1 and 3 of ALMA Partnership et al. (2015) for observed fluxes and noise levels). The CO (5-4) velocity cubes were binned to a velocity resolution of 21 km s^{-1} (ALMA Partnership et al. 2015).

We use the source plane reconstructed images of continuum emissions (in ALMA Bands 4, 6 and 7, corresponding to $\lambda_{\text{obs}} = 2.0, 1.3$ and 1.0 mm , respectively) and CO (5-4) flux and velocity, created by S15, using the lensing model by Dye et al. (2015). This model was used in the image plane with the semi-linear inversion method (Warren & Dye 2003) worked upon by Nightingale & Dye (2015). The average luminosity weighted magnification factors derived by Dye et al. (2015) for the continuum in band 6 and 7 are 15.8 ± 0.7 and 16.0 ± 0.7 respectively. This magnification is representative of a higher resolution by a factor of ~ 30 (sub-kpc scale) than that in the typical non-lensed case (Ikarashi et al. 2015; Simpson et al. 2015).

S15 identified 5 molecular clumps from the continuum emission maps where intense star formation is taking place (see Figure 1 in their paper), using a signal to *local* noise (SNR) cutoff at 5σ . Of these clumps, only clumps A and B have sufficient resolution (number of pixels) to perform the kinematic analysis to estimate the turbulent velocity dispersion (see Figure 1). The horizontally elongated structure of clump B rules out the possibility of a spherical approximation to its volume which we otherwise cannot estimate, not to mention that its location does not correlate well with the CO (5-4) flux map. Clump A, on the other hand, has a strong correlation with CO (5-4) flux and appears symmetric, as seen in Figure 1. Hence, we restrict our analysis to clump A in this work. We notice that clump A likely coincides with the center of the galaxy and might be its nucleus/forming core. Thus, it might be significantly different in origin from clumps residing in the outer regions of the disk.

3 MEASUREMENT OF THE STAR FORMATION RATE

We estimate the SFR surface density (Σ_{SFR}) in clump A by fitting a modified blackbody (MBB) spectrum to the continuum emission from dust in the three ALMA bands. The modified blackbody spectral law can be written as:

$$S_{\nu} = N_{\nu} \left(\frac{2h\nu^3}{c^2} \right) \frac{1}{e^{h\nu/k_{\text{B}}T} - 1} \nu^{\beta_{\text{em}}}, \quad (1)$$

where ν is the rest-frame frequency, S_{ν} is the flux density of the clump, N_{ν} is the normalization parameter (includes dust opacity), T is the dust temperature and β_{em} is

¹ <https://almascience.nao.ac.jp/alma-data/science-verification>

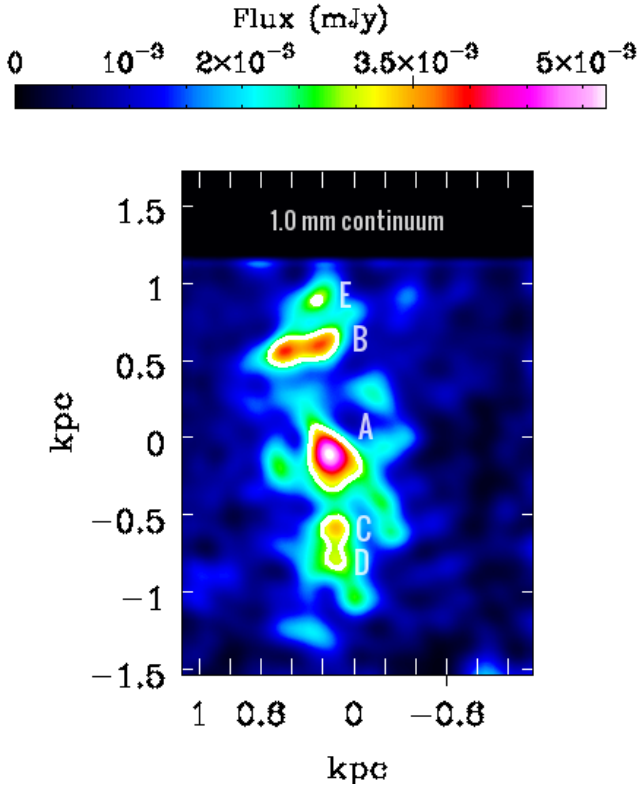


Figure 1. Source reconstructed image of continuum flux in ALMA band 7 ($\lambda_{\text{obs}} = 1.0$ mm), created using CASA (McMullin et al. 2007). The contours depict clumps A, B, C, D and E, taken from Figure 1 of S15. We do not use clumps B, C, D and E in this work because they do not allow for accurate estimates of kinematics and volume densities from the plane-of-the-sky projection.

the emissivity index ($\beta_{\text{em}} = 0$ corresponds to a blackbody) (Draine & Lee 1984; Da Cunha et al. 2010b). Since clump A lies near the center of the galaxy where the background contribution may be high, we subtract the underlying (disc) CO emission from clump A. For background subtraction, we mask the clump A and then smooth the image by convolving it with a large Gaussian kernel. Then, we subtract the smoothed image from the original image to get the background subtracted image. In order to ensure that we do not over or under-subtract, we reiterate this procedure multiple times with different kernels.

The flux density can be integrated over the whole infrared (IR) range (8–1000 μm) to get dust luminosity (Hugson et al. 1956; Oke & Sandage 1968; Hogg et al. 2002):

$$L_{\text{FIR}} = \frac{4\pi D_{\text{L}}^2}{1+z} \int_{8\mu\text{m}}^{1000\mu\text{m}} S_{\nu} d\nu, \quad (2)$$

where L_{FIR} is the far infrared luminosity of the clump, D_{L} is the luminosity distance to SDP 81 and S_{ν} is the flux density of the clump. However, the available ALMA observations are insufficient to simultaneously constrain the dust parameters – T , β_{em} , and L_{FIR} . Therefore, we fix $\beta_{\text{em}} = 1.5, 2.0$ and 2.5 , which are the typically used values for starburst galaxies (Hildebrand 1983; Blain et al. 2003; Casey 2012; Smith et al. 2013). We also include observed fluxes at various other wavelengths in the infrared regime, reported in Table

2 of Negrello et al. (2014), which covers a longer wavelength baseline ($\lambda_{\text{obs}} = 350 - 2000$ mm). Then, using a two-step fitting process: 1.) we fit the galaxy-integrated fluxes to constrain T and β_{em} ; 2) we then adopt the ‘galaxy-wide’ T and β_{em} to fit clump A and determine its far infrared luminosity. The conditions of individual clumps might be very different as compared to the whole galaxy. We lack the spatial resolution for a proper decomposition of the various clumps and assume that the clump conditions (of clump A) are identical to the galaxy-wide properties, while being aware that this might not be the case. We include the systematic uncertainty arising from this assumption in our calculation of the far infrared luminosity.

We derive a best-fit temperature $T = 39 \pm 2$ K for $\beta_{\text{em}} = 2.5$, where we use Monte Carlo (MC) simulations (by modeling the uncertainties in the observed fluxes according to a Gaussian distribution) to find the bestfit MBB (Ogilvie 1984; Johnson et al. 2013). The uncertainty on T arises from the inclusion of the flux at $350 \mu\text{m}$ (from SPIRE observations, Griffin et al. 2010) which falls partially under the cold temperature dominated regime (see Figure 6 of Dye et al. 2015). Figure 2 shows the best-fit MBB we find for clump A from the fits, along with the 1σ uncertainty range we derive from the 1σ uncertainty of the far infrared luminosity (L_{FIR}) obtained using MC error propagation.

We obtain nearly identical values of (T, β_{em}) from the two fitting methods we use: pixel-by-pixel and whole clump. In the pixel-by-pixel algorithm, we find the SFR in each pixel by fitting the MBB using the best-fit (T, β_{em}) values. Then, we sum the SFRs from each pixel to get SFR for the whole clump. On the contrary, in the whole clump fitting algorithm, we first sum the fluxes from each pixel and then find the SFR by fitting the MBB using the best-fit (T, β_{em}) values. The SFRs we obtain from both the methods agree well with each other, within $\pm 3\%$.

Using equation 2, we derive $L_{\text{FIR}} = (2.25_{-0.47}^{+0.95}) \times 10^{11} L_{\odot}$ for clump A, where the uncertainty includes statistical as well as systematic errors. The observed SFR surface density we find using the $L_{\text{FIR}} - \text{SFR}$ relation from Kennicutt (1998a) is $\Sigma_{\text{SFR}} = 555_{-120}^{+197} \text{M}_{\odot} \text{yr}^{-1} \text{kpc}^{-2}$. Since this relation used a Salpeter IMF (Salpeter 1955), we adjust its coefficient by a factor of 1.6 downward to adopt to ‘the Chabrier IMF’ (Chabrier 2003) to be consistent throughout our work (Da Cunha et al. 2010a,b). The resulting SFR surface density we get is $\Sigma_{\text{SFR}} = 357_{-85}^{+135} \text{M}_{\odot} \text{yr}^{-1} \text{kpc}^{-2}$. These values are representative of intense star formation and are expected for the central regions of high-redshift starburst galaxies (Cibinel et al. 2017; Cañameras et al. 2017).

To reinforce our estimation of flux densities in the three ALMA bands as obtained after background subtraction, we also model the fluxes using an n-Sérsic profile ($R^{1/n}$) for the disc, with a Gaussian added to it for clump A (Sersic 1968; Caon et al. 1993; Ciotti & Bertin 1999; Trujillo et al. 2001; Aceves et al. 2006). The Sérsic index (n) we obtain for $\lambda_{\text{obs}} = 1.0$ mm continuum is $n \sim 0.5$. Although our result is lower than the median value reported in Hodge et al. 2016 ($n \approx 1 \pm 0.2$, see also Paulino-Afonso et al. 2018), it is consistent with the Sérsic indices found in several high-redshift galaxies (see Table 1 of Hodge et al. 2016). Through this composite profile, the fluxes we obtain for clump A for the three bands are similar to those obtained through background subtraction discussed above, within $\pm 12\%$. Since this

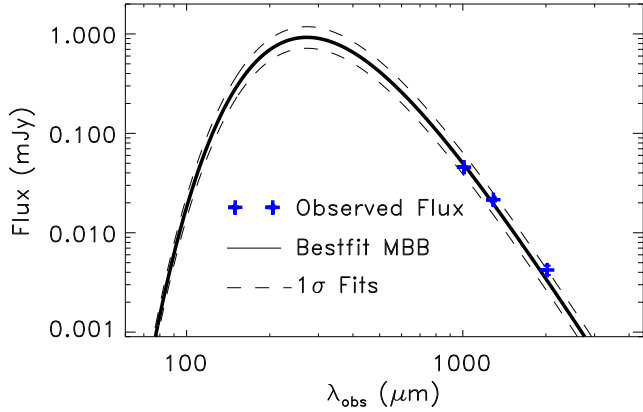


Figure 2. SED fit applied to clump A with $T = 39$ K, $\beta_{\text{em}} = 2.5$ (parameters obtained from SED fit of data from SPIRE (Griffin et al. 2010), SMA (Bussmann et al. 2013), MAMBO (Negrello et al. 2010) and ALMA (ALMA Partnership et al. 2015)). Observed fluxes for the three ALMA bands are shown in blue. Dashed lines indicate the 1σ uncertainty range of the fit.

difference in flux densities is negligible, the resulting L_{FIR} and Σ_{SFR} from this method are similar to those quoted above, within the uncertainties.

3.1 Gas Mass and Clump Size from Continuum Emission

Apart from the SFR surface density, one can also estimate the gas mass (M_{gas}) and size of the clump (R) using the SED fits and continuum maps, respectively. Since we have an excellent coverage of the Rayleigh-Jeans regime, we use our best-fit MBB to estimate the dust mass of clump A by using equation 6 of Magdis et al. (2012) and appropriate rest-frame dust mass absorption coefficients for the three ALMA bands, from Table 6 of Li & Draine (2001). Then, we use a typical gas-to-dust conversion ratio of 150 to get the gas mass in this clump (Dunne et al. 2000; Dye et al. 2015; Brisbin et al. 2017). For the three ALMA bands, the gas masses we thereby obtain are $M_{\text{gas}} = (2.3 - 4.9) \times 10^8 M_{\odot}$. This is consistent with the value of M_{gas} we obtain from CO (5-4) (as we discuss in detail in Section 5).

We use the composite disc profile (n-Sérsic disc + Gaussian clump, as discussed in Section 3) to find an estimate of the size of clump A. Since the clump is defined using the $\lambda_{\text{obs}} = 1.0$ mm continuum obtained from ALMA, we use the best-fit composite disc profile at this wavelength and find the size of this clump by assuming that its diameter is equal to the full width at half maximum of the composite profile (i.e., $\text{FWHM} = 2R$). Correspondingly, we obtain $R \sim 0.16$ kpc for clump A. This is in good agreement with the size of clump A we find in Section 5 by summing up the pixels belonging to clump A, as we report in Table 1.

4 MACH NUMBER ESTIMATION

Supersonic turbulence is a key ingredient to star formation because it can compress interstellar gas which leads to the formation of dense cores. On the other hand, it can suppress

the global collapse of the clouds, thus significantly reducing the SFR (Elmegreen & Scalo 2004; Mac Low & Klessen 2004; McKee & Ostriker 2007; Hennebelle & Falgarone 2012). The root mean square (RMS) sonic Mach number associated with turbulence in star-forming regions is given by:

$$\mathcal{M} = \frac{\sigma_{v,\text{turb}}}{c_s}, \quad (3)$$

where $\sigma_{v,\text{turb}}$ is the turbulent velocity dispersion and c_s is the sound speed. $c_s \propto \sqrt{T}$, where T is the gas temperature. It is difficult to estimate the gas temperature with the current data, however, we can assume it to be between 10–100 K. This assumption is valid for gas temperatures in dense molecular clouds (Gao & Solomon 2004; Solomon & Vanden Bout 2005; Wu et al. 2005; Battersby et al. 2014; Immer et al. 2016; Krieger et al. 2017). Using the relation for isothermal sound speed from Federrath et al. (2016) for a mean molecular weight of 2.33 (Kauffmann et al. 2008) and $T_{\text{gas}} \approx 10$ K, the sound speed is ~ 0.2 km s $^{-1}$ whereas it is ~ 0.6 km s $^{-1}$ for $T_{\text{gas}} \approx 100$ K; so we assume the sound speed to be in the range 0.2 – 0.6 km s $^{-1}$.

The CO (5-4) velocity map after source plane reconstruction shows a clear, large-scale gradient running diagonally, as we show in Figure 3 (also, Figure 1 of S15). This systematic gradient can be associated with the rotational or shear motion of the gas. To extract the small-scale turbulent features in this clump, we fit a large-scale gradient to the clump and subtract it; similar to the analysis of turbulent velocity dispersion done on the central molecular zone (CMZ) cloud Brick by Federrath et al. (2016). For this purpose, we use the PLANEFIT routine in IDL which performs a least-squares fit of a plane to set of (x, y, z) points. In this case, this set is a position-position-velocity (PPV) cube with x and y being the position coordinates of pixels forming clump A, and z being the CO (5-4) velocity of each pixel. We use the standard deviation of residuals after gradient subtraction as the turbulent velocity dispersion:

$$\sigma_{v,\text{turb}} = \sqrt{\frac{1}{N-1} \sum_{i=1}^N \left((v_{\text{bgs}} - v_{\text{fg}}) - \mu \right)^2}, \quad (4)$$

where N is the number of pixels or resolution elements, v_{bgs} is the pixel velocity before gradient subtraction, v_{fg} is the velocity of the fitted gradient and μ is the mean of residuals after gradient subtraction (i.e., $\mu = \langle (v_{\text{bgs}} - v_{\text{fg}}) \rangle$).

The turbulent velocity before subtracting the gradient is $\sigma_{v,\text{bgs}} = 80 \pm 10$ km s $^{-1}$. From the gradient subtraction algorithm, we obtain the turbulent velocity dispersion in clump A as $\sigma_{v,\text{turb}} = 37 \pm 5$ km s $^{-1}$, where the 1σ error is the standard deviation calculated using (Lehmann & Casella 1998):

$$s_{\sigma_v} = \sigma_v \cdot \frac{\Gamma(\frac{N-1}{2})}{\Gamma(\frac{N}{2})} \cdot \sqrt{\frac{N-1}{2} - \left(\frac{\Gamma(\frac{N}{2})}{\Gamma(\frac{N-1}{2})} \right)^2}, \quad (5)$$

where $\Gamma(N)$ is the Gamma function. We also find the uncertainty on $\sigma_{v,\text{turb}}$ through MC simulations and note that the result is consistent with the value we obtain from the analytical equation, within $\pm 8\%$. Figure 3 shows the velocity field across clump A before gradient subtraction, fitted

gradient velocities and velocity field after gradient subtraction. By construction, the residuals after gradient subtraction are evenly spread around 0, as is also clear from the PDF of $\sigma_{v,\text{turb}}$ plotted in Figure 4. From Figure 4, we note that the distribution of velocities (in the pixels of clump A) before gradient subtraction is highly non-Gaussian and bimodal, while that of the velocities after gradient subtraction is more consistent with a Gaussian distribution. However, due to low-number statistics, it is hard to infer much information from this distribution; some non-Gaussian contributions may still remain after gradient subtraction, because it only removes the largest-scale mode of systematic shear or rotation. Nonetheless, this distribution is in agreement with velocity PDFs obtained for simulations of supersonic turbulence which are also Gaussian in nature (Klessen 2000; Federrath 2013) and the non-Gaussian components can arise from small-scale rotational or shear modes, or due to the intrinsic features of turbulence (see Section 3.2.2 of Federrath et al. (2016) and references therein). Additionally, we note that the width of the Gaussian we fit for the PDF of velocities after gradient subtraction matches well with what we find using the data (i.e., $\sigma_{v,\text{turb}}(\text{fit}) \approx \sigma_{v,\text{turb}}(\text{data})$).

We also note that the turbulent velocity dispersion we calculate is in agreement with the velocity dispersion of $30 \pm 9 \text{ km s}^{-1}$ calculated by S15 for this clump using the 2nd moment map (i.e., the dispersion along the line of sight, after correction for beam smearing). The velocity dispersion we calculate is in the plane of the sky. A consensus between velocity dispersions using the two methods imply that clump A can be considered isotropic and it is fair to approximate it as a sphere.

Using this turbulent velocity dispersion, we obtain a turbulent Mach number $\mathcal{M} = 96 \pm 28$. Although this is quite high compared to nearby galaxies (see Kennicutt & Evans (2012) and references therein), it falls in the range of Mach numbers associated with starburst galaxies (Gao & Solomon 2004; Bouché et al. 2007; Cresci et al. 2009; Förster Schreiber et al. 2009; Tacconi et al. 2010). Given the high redshift of SDP 81 and previous works highlighting intense star formation, it is not unusual to obtain Mach numbers near 100. In fact, it implies that the role of turbulence becomes more important at the epoch near the maximum star formation in the history of the Universe (Springel & Hernquist 2003; Madau & Dickinson 2014; Falgarone et al. 2017).

4.1 Resolution Check for Gradient Fit and Subtraction Algorithm

The gradient fit and subtraction algorithm works accurately only if the resolution is sufficient. For the CMZ cloud Brick, the resolution scale was in sub-parsecs (Federrath et al. 2016) whereas it is in sub-kiloparsecs for SDP 81. We check if the low number of resolution elements in our data affects our measurements, since the velocity dispersion calculated might vary by more than 20% if sufficient number of pixels are not available to resolve the clump. To investigate whether we have enough pixels to be operating in the saturated regime (where velocity dispersion does not change by more than 20% when the number of resolution elements are altered), we perform a resolution degradation on clump A by creating artificial 'superpixels' (merging nearby pixels to

make a bigger pixel) and then applying the gradient fit subtraction algorithm.

For the first degradation (1/4 resolution), we merge four nearby pixels into one (making a square shape, see Figure 5). While the center of a superpixel is the centroid of the four constituent pixels, its CO (5-4) velocity is the flux-weighted average of CO (5-4) velocities in the constituent pixels:

$$v_{\text{spix}} = \left(\frac{\sum_{i=1}^4 (S_i v_i)}{\sum_{i=1}^4 S_i} \right), \quad (6)$$

where v_{spix} is the velocity of the superpixel, S_i is the flux of the i^{th} constituent pixel and v_i is its velocity. At places where pixels belonging to the clump A cannot make a square by themselves, we use pixels from outside the clump, but mask their flux to be 0. Thus, for such constituent pixels, $S_i = 0$, so these pixels do not contribute to the sums in equation 6.

We do this process twice: decreasing the resolution to (1/4) and (1/16) of the original resolution. This results in a total of 11 and 4 superpixels after the first and second resolution degradation, respectively. Figure 6 shows the turbulent velocity dispersions we get at the three resolutions. We fit a growing exponential of the form $A_0(1 - e^{-N/N_0})$ (where, N is the number of resolution elements) to this data. Since decreasing the resolution by (1/4) does not alter the velocity dispersion by $\gtrsim 20\%$ (as we notice from Figure 6), we confirm that we have enough pixels to resolve this clump with acceptable accuracy.

5 GAS MASS AND FREEFALL TIME FROM CO (5-4)

The total gas mass is an essential parameter which goes in all the star formation relations we test in a later section (see Section 6). It can be estimated by following the CO (1-0) emission in the star-forming region (Carilli & Blain 2002; Pety et al. 2013; McNamara et al. 2014; Scoville et al. 2017). From Figure 1 in Rybak et al. (2015b), and that in Dye et al. (2015), we notice that there is a significant presence of CO (1-0) emission at the position of clump A. However, the CO (1-0) data was obtained by the Karl G. Jansky Very Large Array (VLA) at a lower resolution than ALMA (Valtchanov et al. 2011) and cannot be used for kinematic analysis. Thus, we rely on ALMA observations of CO (5-4) transition (observed at a frequency of 142.57 GHz in ALMA Band 4), to estimate the gas mass of clump A. It should be noted that CO (5-4) is generally a poor tracer of the total diffuse molecular gas, but is bright and easily observable at high redshift (Daddi et al. 2015; Lu et al. 2015; Yang et al. 2017).

We follow the Solomon et al. (1992a,b) relation between line luminosity and integrated flux density of CO (5-4):

$$L'_{\text{CO}(5-4)} = 3.25 \times 10^7 S_v \Delta v \frac{D_L^2}{v_{\text{obs}}^2 (1+z)^3}, \quad (7)$$

where $L'_{\text{CO}(5-4)}$ is the line luminosity in $\text{K km s}^{-1} \text{ pc}^2$, $S_v \Delta v$ is the velocity integrated flux density of CO (5-4) after subtraction of background emission, in Jy km s^{-1} , D_L is

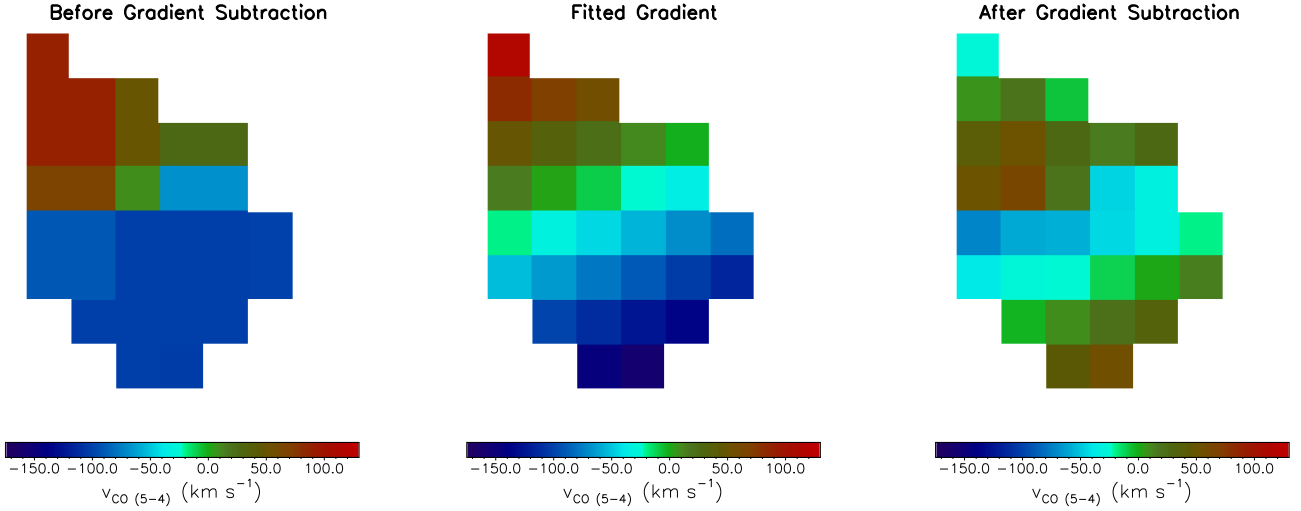


Figure 3. *Left Panel:* Centroid CO (5-4) velocity (in km s^{-1}) in the pixels of clump A before gradient subtraction. The size of each pixel is ~ 0.05 kpc. *Middle Panel:* Fitted large-scale gradient to the clump. *Right Panel:* Velocity of CO (5-4) in the clump after gradient subtraction. The last panel isolates the turbulent velocities in the plane of the sky. The turbulent velocity dispersion obtained for clump A is $\sigma_{v,\text{turb}} = 37 \pm 5 \text{ km s}^{-1}$, using which the Mach number calculated is $\mathcal{M} = \sigma_{v,\text{turb}}/c_s = 96 \pm 28$.

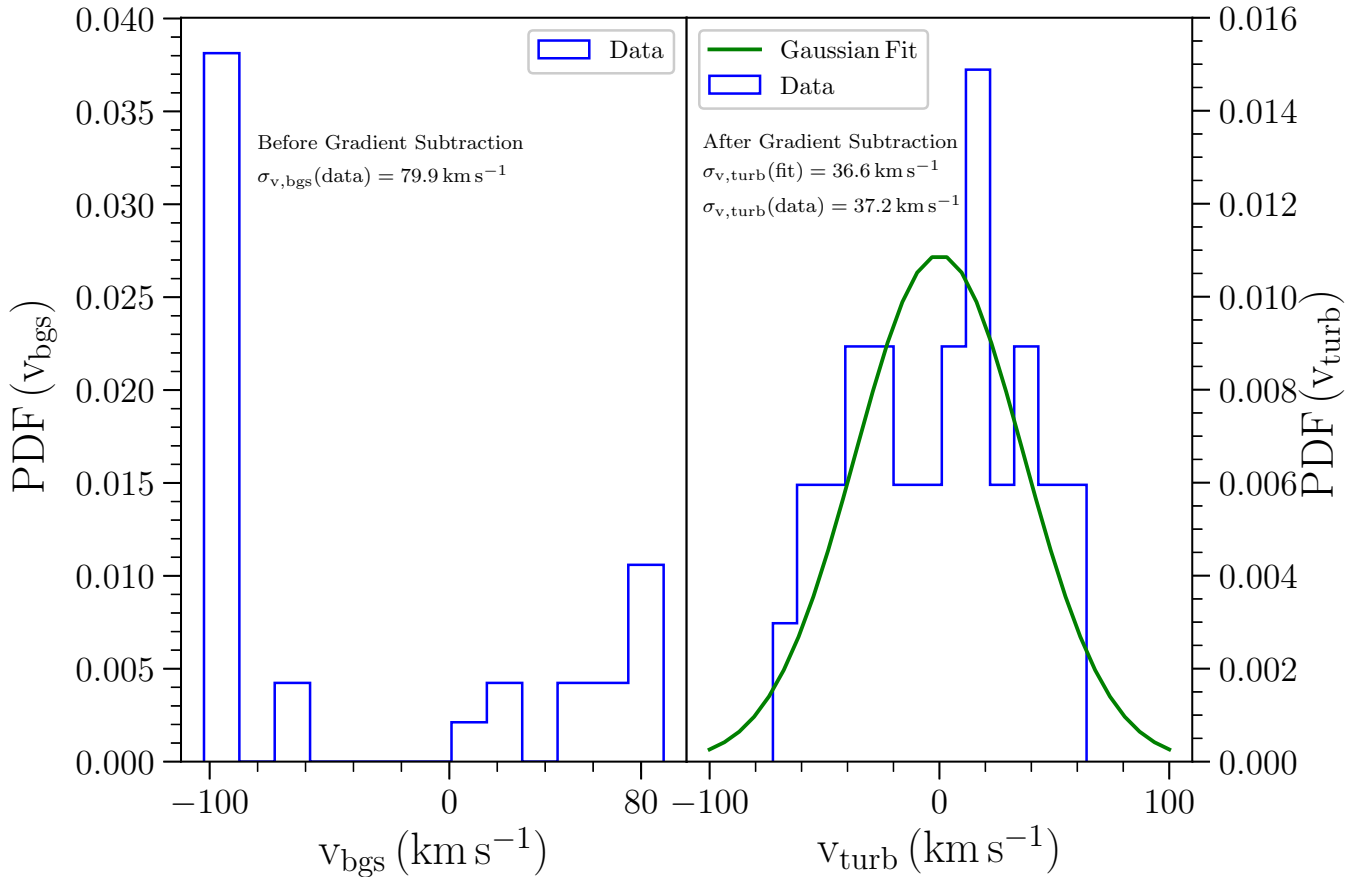


Figure 4. PDFs of CO (5-4) velocities of the pixels in clump A before and after gradient subtraction. The distribution of velocities before gradient subtraction (v_{bgs}) is bimodal; that of velocities after gradient subtraction (v_{turb}) resembles a Gaussian distribution, however, much information cannot be ascertained due to low number of statistics. The width of the Gaussian we fit (right panel) and the data are similar, thus reinforcing the estimate of turbulent velocity dispersion $\sigma_{v,\text{turb}} = 37 \pm 5 \text{ km s}^{-1}$.

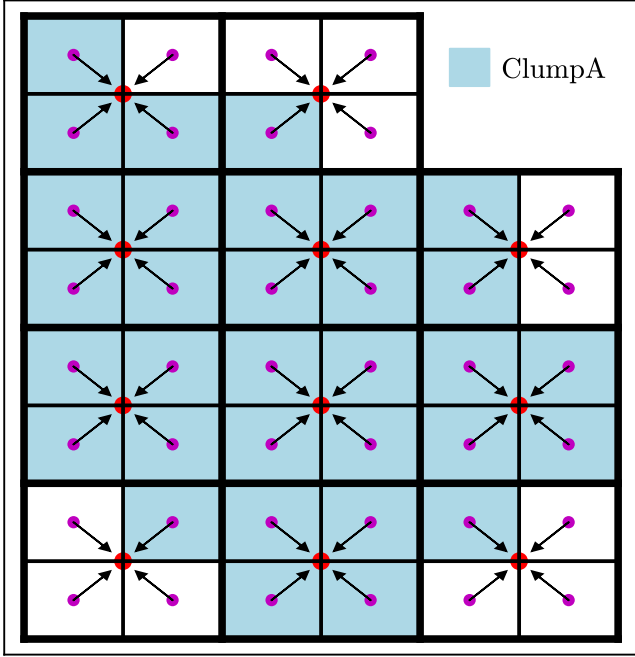


Figure 5. First resolution degradation through creation of 11 superpixels, by merging nearby pixels using a flux-weighted averaging method (see equation 6). Thick lines denote the boundaries of superpixels whereas thinner lines denote the boundaries of pixels. Red dots depict the center of superpixels and purple dots depict the center of pixels. Pixels belonging to clump A are shown in blue; they are the same as those shown in Figure 3. Pixels outside the clump are shown in white. Arrows show the movement of a pixel when it is merged with other pixels to create a superpixel.

the luminosity distance in Mpc and ν_{obs} is the observed frequency of transition in GHz. The line luminosity we obtain is $L'_{\text{CO}(5-4)} = (5.04 \pm 1.10) \times 10^8 \text{ K km s}^{-1} \text{ pc}^2$. Since the transition we observe with ALMA at $z \approx 3$ is higher than the ground (1-0) transition, we introduce an appropriate line ratio factor (defined as the ratio of line luminosity of CO (5-4) to that of CO (1-0)), $r_{54} = 0.28 \pm 0.05$. This value was derived for clump A by S15, where the authors use velocity and magnification maps from the lens model prepared by Dye et al. (2015). This value falls in the typical range of values of r_{54} for SMGs (see Carilli & Walter (2013) and references therein).

To get the gas mass from the line luminosity, we use an appropriate CO to H₂ conversion factor α_{CO} . Although there is a high uncertainty in the value of this factor for nearby as well as high-redshift galaxies (Papadopoulos et al. 2012; Narayanan et al. 2012), the suggested values based on observations of SMGs lie in the range $\sim 0.8\text{--}1.0 M_{\odot}$ per $(\text{K km s}^{-1} \text{ pc}^2)$ (Downes & Solomon 1998; Solomon & Vanden Bout 2005; Tacconi et al. 2008; Magdis et al. 2011; Hodge et al. 2012; Carilli & Walter 2013; Bolatto et al. 2013; Bothwell et al. 2013), which is less by a factor of ~ 4 than the typical value used for Milky Way clouds and nearby galaxies. Dye et al. (2015) used a conversion factor of unity (in the same units) for SDP 81, while Hatsukade et al. (2015) used a value of 0.8. Further, we notice that clump A falls on top of the starburst sequence of the $\Sigma_{\text{gas}} - \Sigma_{\text{SFR}}$ relation populated by local ultra-luminous infrared galaxies (ULIRGs)

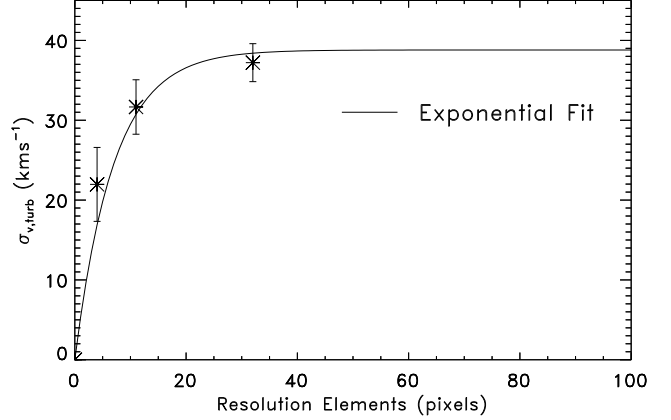


Figure 6. Turbulent velocity dispersion at different resolutions, fitted with a growing exponential function of the form $A_0(1 - e^{-N/N_0})$, where N is the number of resolution elements. $N_0 \sim 7$ for the best fit model, which implies the velocity dispersion does not change by more than 5% for $N \gtrsim 20$.

and SMGs (Daddi et al. 2010). This further justifies the choice of $\alpha_{\text{CO}} \sim 0.8 - 1 M_{\odot}$ per $(\text{K km s}^{-1} \text{ pc}^2)$.

Keeping these studies in mind, we assume $\alpha_{\text{CO}} \approx 0.9 \pm 0.2 M_{\odot}$ per $(\text{K km s}^{-1} \text{ pc}^2)$, which suggests an H₂ mass of $(4.5 \pm 1.0) \times 10^8 M_{\odot}$ ². Accounting for the contribution to the gas by He, we further increase the H₂ mass obtained so far by 36% to get the total gas mass for clump A as $(6.2 \pm 1.4) \times 10^8 M_{\odot}$. This value is in good agreement with the gas mass found out using SED fitting in Section 3. The gas surface density we derive is $\Sigma_{\text{gas}} = (8.6 \pm 1.9) \times 10^9 M_{\odot} \text{ kpc}^{-2}$, where we calculate and sum the area of all pixels which constitute clump A³. Moreover, the size of clump A we obtain in this manner is $R \sim 0.15 \pm 0.02 \text{ kpc}$, in excellent agreement with the size we find through composite disc profile fitting in Section 3.1. Assuming clump A to be spherical (see section 4 for a discussion on the validity of this assumption), we calculate its density to be $\rho = M_{\text{gas}}/V = (2.9 \pm 0.6) \times 10^{-21} \text{ g cm}^{-3}$, where V is the volume of the spherical clump.

To establish whether the cloud could be collapsing, we estimate the virial parameter α_{vir} , which is the ratio of twice the kinetic energy to the gravitational energy (Federrath & Klessen 2012). Using the definition from Bertoldi & McKee (1992), the virial parameter can also be given by:

$$\alpha_{\text{vir}} = \frac{5\sigma_{\text{v,tot}}^2}{4\pi GR^2\rho}, \quad (8)$$

where, the velocity dispersion σ_{tot} is the total thermal and turbulent velocity dispersion including the shear component (*i.e.*, turbulent velocity dispersion before gradient subtraction, $\sigma_{\text{v,bgs}}$). However, in this clump, since the turbulent velocity dispersion $\sigma_{\text{v,bgs}} \gg c_s$, it implies that the total velocity dispersion can be approximated as $\sigma_{\text{v,tot}} \approx \sigma_{\text{v,bgs}}$

² This gas mass is essentially in agreement as that obtained by S15 for clump A. However, due to a typographical error, the gas masses reported in the last column of table 1 of S15 have to be rearranged. The gas masses reported are in the order D-C-A-B-E.

³ The size of 1 pixel is $\sim 0.05 \text{ kpc}$. There are 32 pixels in this clump.

(Krumholz & McKee 2005; Federrath & Klessen 2012). The virial parameter we thus obtain is $\alpha_{\text{vir}} = 0.63 \pm 0.13 < 1$, implying the cloud is strongly gravitationally bound and likely undergoing collapse. For such a cloud, the freefall time can be given by (Hennebelle & Chabrier 2011, 2013; Chabrier et al. 2014):

$$t_{\text{ff}} = \sqrt{\frac{3\pi}{32G\rho}}, \quad (9)$$

where G is the gravitational constant. From this equation, we obtain a freefall time of 1.3 ± 0.1 Myr. This value is in agreement with freefall times calculated for other high z starbursts (see Table 4 of Krumholz et al. 2013).

We summarize all the parameters going into predictions of SFR surface density in various star formation relations in Table 1.

6 COMPARISON OF OBSERVED SFR SURFACE DENSITY WITH THEORETICAL PREDICTIONS BY K98, KDM12 AND SFK15

We compare the SFR surface density obtained through dust SED fitting with star formation relations proposed for nearby and high-redshift galaxies in Figure 7. The probability density function (PDF) of the measured SFR surface density in clump A is shown as the solid line, and we compare it with the predictions of SFR surface density by three popular star formation relations in the same plot. These PDFs were calculated using Monte Carlo simulations with a sample size of 100,000 and included systematic errors on the SFR surface densities.

The Kennicutt-Schmidt (KS or K98) relation is given by (Schmidt 1959; Kennicutt 1998b):

$$\Sigma_{\text{SFR}} = 2.53 \times 10^{-4} \Sigma_{\text{gas}}^{1.4 \pm 0.15}, \quad (10)$$

The distribution of SFR surface density (Σ_{SFR}) obtained using equation 10 is shown as the dotted line in Figure 7. The mean SFR surface density we calculate from the KS relation is $\Sigma_{\text{SFR}} = 84 \pm 27 \text{ M}_{\odot} \text{ yr}^{-1} \text{ kpc}^{-2}$. Since equation 10 is based on the Salpeter IMF, we correct the SFR surface density for a Chabrier IMF (similar to that done in section 3) and obtain $\Sigma_{\text{SFR}} = 52 \pm 17 \text{ M}_{\odot} \text{ yr}^{-1} \text{ kpc}^{-2}$.⁴ We find that the KS relation underestimates SFR surface density by a factor $\gtrsim 3.3$, with respect to the observed SFR surface density in this clump, even when the 1σ uncertainty is taken into account. Numerous studies discuss the breakdown of the KS relation on the scales of $\sim 100 \text{ pc}$ in local (Onodera et al. 2010; Shi et al. 2011; Becerra & Escala 2014; Xu et al. 2015) and high-redshift environments (Bouché et al. 2007; Daddi et al. 2010; Genzel et al. 2010).

Krumholz, Dekel and McKee (KDM12) showed that the SFR does not only depend on gas surface density but also

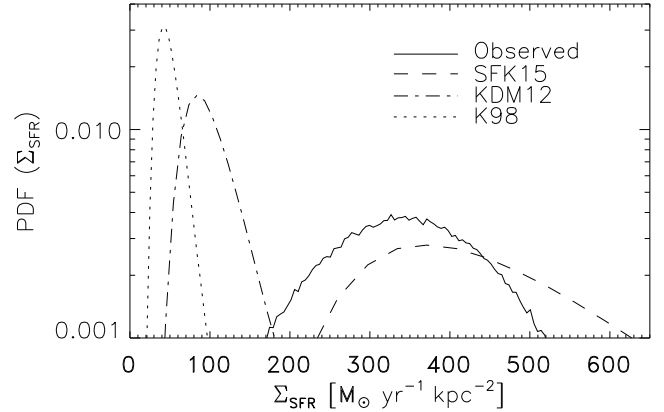


Figure 7. Probability distribution function (PDF) of Σ_{SFR} estimated from dust SED fitting (solid curve) and those predicted from K98 (dotted curve, equation 10), KDM12 (dot-dashed curve, equation 11) and SFK15 (dashed curve, equation 12) relations. The PDFs were calculated using MC simulations with a sample size of 100,000.

Table 1. Results for Clump A in SDP 81 (see Figure 1) with mean and 1σ errors.

Parameter	Value
β_{em}	2.5
T	$39 \pm 2 \text{ K}$
L_{FIR}	$(2.3^{+1.0}_{-0.5}) \times 10^{11} L_{\odot}$
$\Sigma_{\text{SFR}} \text{ (observed)}^{\text{a}}$	$357^{+135}_{-85} \text{ M}_{\odot} \text{ yr}^{-1} \text{ kpc}^{-2}$
A	$(7.2 \pm 1.5) \times 10^{-2} \text{ kpc}^2$
R	$(1.5 \pm 0.2) \times 10^{-1} \text{ kpc}$
$\sigma_{\text{v,bgs}}^{(\text{b})}$	$80 \pm 10 \text{ km s}^{-1}$
$\sigma_{\text{v,turb}}^{(\text{c})}$	$37 \pm 5 \text{ km s}^{-1}$
c_{s}	$0.4 \pm 0.2 \text{ km s}^{-1}$
\mathcal{M}	96 ± 28
b	0.4
$S_{\text{v,CO}(5-4)}^{(\text{d})}$	$8.4 \pm 1.8 \text{ mJy km s}^{-1}$
$L'_{\text{CO}(1-0)}$	$(1.4 \pm 0.1) \times 10^8 \text{ K km s}^{-1} \text{ pc}^2$
r_{54}	0.28 ± 0.05
$L'_{\text{CO}(5-4)}$	$(5.0 \pm 1.1) \times 10^8 \text{ K km s}^{-1} \text{ pc}^2$
α_{CO}	$0.9 \pm 0.2 \text{ M}_{\odot} (\text{K km s}^{-1} \text{ pc}^2)^{-1}$
M_{gas}	$(6.2 \pm 1.4) \times 10^8 \text{ M}_{\odot}$
Σ_{gas}	$(8.6 \pm 1.9) \times 10^9 \text{ M}_{\odot} \text{ kpc}^{-2}$
ρ	$(2.9 \pm 0.6) \times 10^{-21} \text{ g cm}^{-3}$
α_{vir}	0.6 ± 0.1
t_{ff}	$(1.3 \pm 0.1) \times 10^6 \text{ yr}$
$\Sigma_{\text{SFR}} \text{ (K98)}^{(\text{a,e})}$	$52 \pm 17 \text{ M}_{\odot} \text{ yr}^{-1} \text{ kpc}^{-2}$
$\Sigma_{\text{SFR}} \text{ (KDM12)}^{(\text{f})}$	$106 \pm 37 \text{ M}_{\odot} \text{ yr}^{-1} \text{ kpc}^{-2}$
$\Sigma_{\text{SFR}} \text{ (SFK15)}^{(\text{g})}$	$491^{+139}_{-194} \text{ M}_{\odot} \text{ yr}^{-1} \text{ kpc}^{-2}$

(a) Corrected for Chabrier IMF.

(b) Large-scale velocity dispersion before gradient subtraction.

(c) Turbulent velocity dispersion after gradient subtraction.

(d) Integrated CO (5-4) flux after background subtraction.

(e) 16th and 84th percentiles are 37 and 64 $\text{M}_{\odot} \text{ yr}^{-1} \text{ kpc}^{-2}$.

(f) 16th and 84th percentiles are 74 and 132 $\text{M}_{\odot} \text{ yr}^{-1} \text{ kpc}^{-2}$.

(g) Errors represent the 16th and 84th percentiles.

⁴ This distribution does not take into account the uncertainty on the power law index in equation 10 because we notice that it becomes highly skewed when this uncertainty is randomized. In that case, the 16th and 84th percentile values of Σ_{SFR} are 1 and 133 $\text{M}_{\odot} \text{ yr}^{-1} \text{ kpc}^{-2}$, respectively.

on the depletion time of the gas under collapse. Their single-freefall time model takes the form:

$$\Sigma_{\text{SFR}} = f_{\text{H}_2} \epsilon_{\text{ff}} \frac{\Sigma_{\text{gas}}}{t_{\text{ff}}}, \quad (11)$$

where f_{H_2} is the fraction of gas available in molecular form (assumed to be unity), and ϵ_{ff} is the SFR per freefall time. They found a best fit $\epsilon_{\text{ff}} = 0.015$ (see Krumholz et al. 2013). The freefall time they used is the minimum of the Toomre timescale (equation 8 in KDM12) and the giant molecular cloud (GMC) freefall time (equation 4 in KDM12). The SFR surface density suggested from KDM12 is $\Sigma_{\text{SFR}} = 106 \pm 37 \text{ M}_{\odot} \text{ yr}^{-1} \text{ kpc}^{-2}$. We plot the PDF of the predicted SFR surface density from KDM12 as the dot-dashed line in Figure 7.

As can be seen from Figure 7, both KS and KDM12 relations underestimate the observed SFR surface density in clump A. In order to match the SFR surface density predicted by the KS or KDM12 relations with that observed, the dust temperature (which goes into the modified black-body function, see equation 1) should be lowered by $\sim 8 \text{ K}$, if emissivity is fixed at the best fit emissivity $\beta_{\text{em}} = 2.5$. Another way could be to decrease the emissivity to 1.9 such that the original best fit temperature ($T = 39 \text{ K}$) can provide a reasonable match of observed SFR surface density with that predicted by KS or KDM12 relations. Although these values of (T, β_{em}) are not favored by the SED fit, they are in the typical range of dust temperature and emissivity found out for other high-redshift galaxies (Smith et al. 2013; Ota et al. 2014; Lu et al. 2015, 2017). Furthermore, in order to fit the KS relation to the observed SFR surface density in this clump, we find that the power law should be steeper with an exponent of $n \approx 1.6$ in equation 10). This is consistent with scaling in the KS relation estimated for other SMG galaxies and starbursts (Bouché et al. 2007; Khoperskov & Vasiliev 2017). Moreover, Daddi et al. (2010) also proposed that the KS relation underpredicts the star formation efficiency in starburst galaxies by a factor of 10. Similarly, an equivalence between observed SFR surface density and that predicted by KDM12 relation can be obtained if ϵ_{ff} in equation 11 is increased to thrice its best fit value. These discrepancies between observed and predicted SFR surface density motivates us to include the role of turbulence in star formation relations, as suggested by SFK15.

The SFK15 relation is the result of the combination of gas surface density and density-dependent freefall time determined by KDM12 (see also Krumholz et al. 2013) and the role of turbulence in star-forming regions (Federrath & Klessen 2012; Federrath 2013). SFK15 was able to correlate the scatter present in the KS relation with turbulent motions in gas clouds and using robust fitting techniques, found that Σ_{SFR} is $\sim 0.45\%$ of the multi-freefall gas consumption rate (MGCR) in star-forming regions:

$$\Sigma_{\text{SFR}} = \left(\frac{0.45}{100} \right) \frac{\Sigma_{\text{gas}}}{t_{\text{ff}}} \left(1 + b^2 \mathcal{M}^2 \frac{\beta_{\text{mag}}}{\beta_{\text{mag}} + 1} \right)^{3/8}, \quad (12)$$

where b is the turbulent driving parameter ($b = 1/3$ for solenoidal driving and $b = 1$ for compressive driving) (Federrath et al. 2008, 2010; Federrath & Klessen 2012; Federrath 2013). We use a mixed driving mode with $b =$

0.4 (Federrath et al. 2010). The turbulence term was derived by Molina et al. (2012). In this term, β_{mag} is the ratio of thermal to magnetic pressure. It can also be expressed as a ratio of Alfvén to sonic Mach numbers: $\beta_{\text{mag}} = 2 \mathcal{M}_A^2 / \mathcal{M}^2$. The freefall time used in this equation comes from $\min(t_{\text{ff,T}}, t_{\text{ff,GMC}})$, where T stands for Toomre and GMC stands for giant molecular clouds, as used by KDM12. KDM12 showed that the Toomre time is shorter than the GMC freefall time for starburst galaxies. We do not have any estimates of magnetic field strength in this galaxy since it requires polarization or Zeeman measurements of the magnetic field, which are unavailable for SDP 81. For simplicity, we neglect magnetic fields and set $\beta_{\text{mag}} \rightarrow \infty$, leading to $\beta_{\text{mag}} / (\beta_{\text{mag}} + 1) = 1$.

The SFK15 relation (equation 12) generates a skewed distribution of predicted SFR surface density, as shown in Figure 7. The mean of the distribution is $\Sigma_{\text{SFR}} = 491_{-194}^{+139} \text{ M}_{\odot} \text{ yr}^{-1} \text{ kpc}^{-2}$, where the errors represent the 16th and 84th percentiles. As can be seen from Figure 7, the distribution of SFR surface density predicted from SFK15 overlaps to a good extent with the distribution of the observed SFR surface density. The overestimation of SFR surface density by SFK15 can be attributed to ignoring the magnetic field strength, which can reduce the SFR by a factor of ~ 2 (Padoan & Nordlund 2011; Federrath & Klessen 2012; Federrath 2015).

Figure 8 depicts the observed SFR surface density (Σ_{SFR}) plotted against gas surface density (Σ_{gas}) and single and multi-freefall times, overlaid with the three star formation relations, consistent with the Chabrier IMF. We also plot other star formation relations based on gas surface density (Bigiel et al. 2008 (B08); Heiderman et al. 2010 (H10); Wu et al. 2010 (W10) and Bigiel et al. 2011 (B11)) in the first panel of Figure 8. While the H10 relation can possibly explain the observed SFR surface density in the clump A in SDP 81, it is not universally applicable. Other star formation relations shown in this panel cannot account for observed SFR surface density in all the molecular clouds. Additionally, we also note that SDP 81 lies on the dashed line in the middle panel of Figure 8, which represent deviations by a factor of 3 from the best fit relation of KDM12 (shown as the solid line). It is evident that there is a large scatter in both the K98 and KDM12 relations, which we calculate from:

$$\chi_{\text{red}}^2 = \frac{1}{N_{\text{D}}} \sum \left(\frac{\Sigma_{\text{SFR}}(\text{observed}) - \Sigma_{\text{SFR}}(\text{predicted})}{E} \right)^2, \quad (13)$$

where E is the measured error on $\Sigma_{\text{SFR}}(\text{observed})$ and N_{D} is the number of star-forming regions⁵. We emphasize that we do not fit any relations to compute the scatter but simply perform a χ^2 minimization routine. From equation 13, we calculate a reduced χ^2 scatter of $\chi_{\text{red}}^2 = 50.1$ and 7.27 for the KS and KDM12 relations, respectively. The final panel in Figure 8 illustrates the turbulence based SFK15 relation. We observe that the characteristics of the clump A in SDP 81 match the SFK15 relation to a good extent. The

⁵ For the calculation of scatter, only those data are included for which $\Sigma_{\text{SFR}}(\text{predicted})$ is available for each of K98, KDM12 and SFK15 relations.

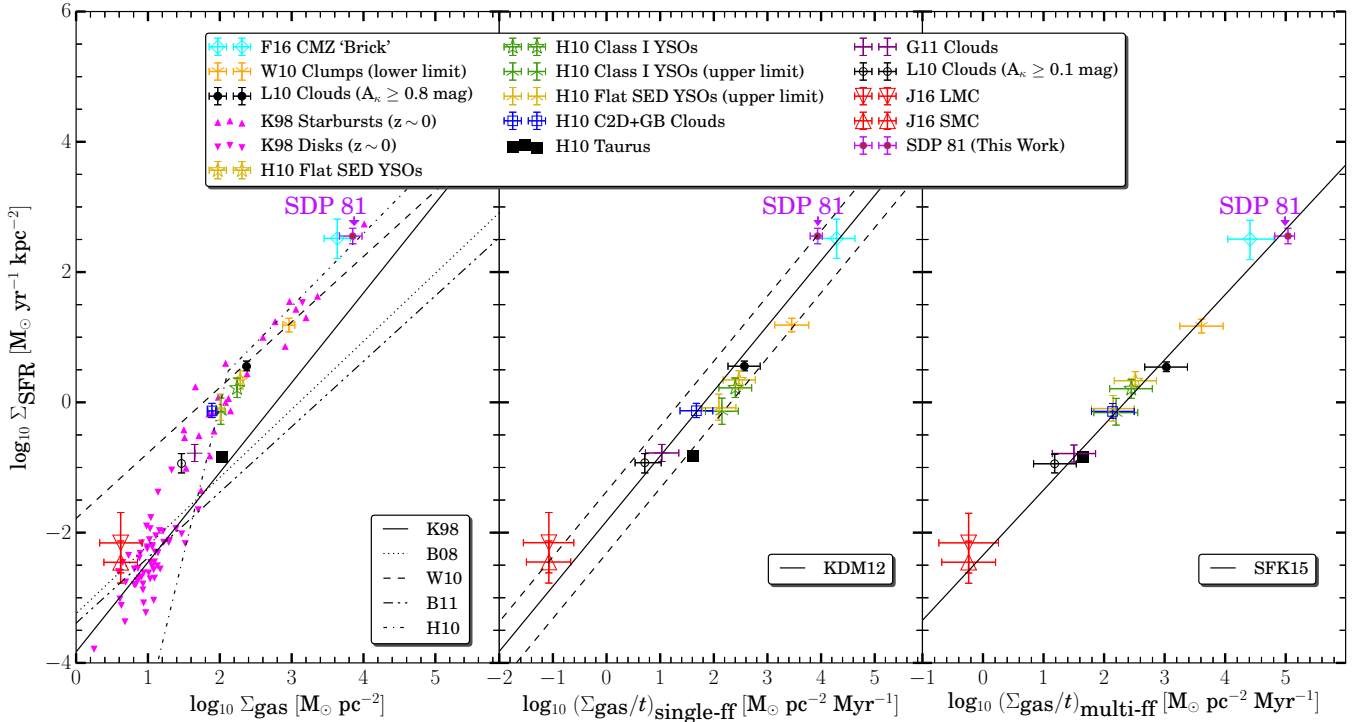


Figure 8. *Left-panel:* Observations of Σ_{SFR} (SFR surface density) in local clouds, plotted against gas surface density. The data is extracted from Heiderman et al. 2010 (H10), Lada et al. 2010 (L10), Wu et al. 2010 (W10), Gutermuth et al. 2011 (G11) and Jameson et al. 2016 (J16). Data for the Brick molecular cloud in the central molecular zone (CMZ) is taken from Federrath et al. 2016 (F16). The K98 (disks and starbursts) data were adjusted in KDM12, Krumholz et al. (2013) and Federrath (2013) to the Chabrier IMF, similar to that done for the high-redshift data by Daddi et al. (2010). The systematic difference between starbursts and the original K98 relation is due to different α_{CO} conversion factors used for starbursts and disks (see Section 2 of Daddi et al. 2010 and Figure 1 of Federrath 2013). SFR relations proposed by Kennicutt 1998b (K98, corrected for Chabrier IMF), Bigiel et al. 2008 (B08), Bigiel et al. 2011 (B11), Wu et al. 2010 (W10) and Heiderman et al. 2010 (H10) are also shown. *Middle-panel:* Observations of Σ_{SFR} plotted against the single-freefall time. Solid line depicts the best fit model from KDM12, with $\epsilon_{\text{ff}} = 0.015$ (see Krumholz et al. (2013)); dashed lines illustrate deviations by a factor of 3 from the best fit. *Right-panel:* Observations of Σ_{SFR} plotted against the turbulence based multi-freefall model proposed by Salim et al. 2015 (SFK15). Solid line represents equation 12. Clump A analyzed in this work is marked with an arrow in all the three panels. The scatter obtained through a χ^2 minimization routine for K98, KDM12 and SFK15 relations is 50.1, 7.27 and 1.25, respectively.

scatter we obtain for the SFK15 relation is 1.25. It has significantly reduced as compared to the scatter from KS and KDM12 relations because the SFK15 relation includes systematic variations in the Mach number, as were established by Federrath (2013). This highlights the role of turbulence in star-forming regions (Federrath & Klessen 2012; Kraljic et al. 2014). The validity of the multi-freefall star formation relation has been previously supported in an independent work by Braun & Schmidt (2015).

7 CONCLUSIONS

Using high-resolution (sub-kpc) ALMA data of SDP 81 – a high-redshift ($z \sim 3$) lensed galaxy, we have measured the SFR surface density in its biggest and most isotropic clump revealed by the lensing analysis of Dye et al. (2015). Through dust SED fitting by a modified blackbody spectrum of this clump (clump A in S15), we find the best fit dust temperature to be 39 K when an emissivity index $\beta_{\text{em}} = 2.5$ is used. We determine the corresponding SFR surface density of this clump as $\Sigma_{\text{SFR}} = 357 \pm 9 \text{ M}_{\odot} \text{ yr}^{-1} \text{ kpc}^{-2}$, which is in the sub-Eddington limit for starburst galaxies at the given

redshift. Taking into account the systematic errors resulting from partially cold temperature dominated flux and assuming that this clump has conditions similar to those in the whole galaxy, we obtain $\Sigma_{\text{SFR}} = 357^{+135}_{-85} \text{ M}_{\odot} \text{ yr}^{-1} \text{ kpc}^{-2}$.

Using CO (5-4) flux and velocity data for this galaxy, we obtain a turbulent velocity dispersion of $\sigma_{\text{v,turb}} = 37 \pm 5 \text{ km s}^{-1}$, corresponding to a turbulent Mach number $\mathcal{M} = 96 \pm 28$. This is somewhat higher than the typical Mach numbers found for local galaxies, but is in agreement with those estimated for high-redshift starbursts. The turbulent velocity dispersion that goes into estimating this Mach number is obtained from large-scale gradient subtraction from the CO (5-4) velocity, which is in good agreement with the velocity dispersion obtained along the line of sight by S15 after correcting for beam smearing. Using an appropriate CO to H_2 conversion factor for this galaxy, we find the gas mass in the clump we study to be $(6.2 \pm 1.4) \times 10^8 \text{ M}_{\odot}$, which is in agreement with that found out using the best-fit modified blackbody function and the dynamical mass obtained for this clump (S15).

On testing star-forming relations based on gas mass, freefall times and turbulence (available in literature), we find that the KS relation underpredicts the observed SFR surface

density in this clump ($\Sigma_{\text{SFR,KS}} = 52 \pm 17 \text{ M}_{\odot} \text{ yr}^{-1} \text{ kpc}^{-2}$) by a factor $\gtrsim 3.3$, which can be corrected for if the dust temperature is lowered while keeping the emissivity the same or vice-versa. It is also clear that the other star formation relations as plotted in first panel of Figure 8 are not universally applicable. Further, the freefall time based KDM12 relation also underestimates the observed SFR surface density in this clump, giving $\Sigma_{\text{SFR,KDM}} = 106 \pm 37 \text{ M}_{\odot} \text{ yr}^{-1} \text{ kpc}^{-2}$; however, it can explain the observed SFR if deviations up to a factor of 3 from its best fit model are considered. We also find that the large scatter present in these star formation relations can be explained by turbulence acting in this clump. The turbulence regulated multi-freefall model by SFK15 predicts the SFR surface density as $\Sigma_{\text{SFR,SFK}} = 491^{+139}_{-194} \text{ M}_{\odot} \text{ yr}^{-1} \text{ kpc}^{-2}$. The overestimation of SFR surface density by SFK15 can be attributed to ignoring magnetic fields while calculating the SFR through equation 12. Our findings emphasize the role of turbulence giving rise to the multi-freefall model of the SFR and its consistency with the observed SFR in molecular clouds in local as well as high-redshift galaxies.

ACKNOWLEDGEMENTS

The authors thank the anonymous referee for comments which significantly helped to improve the paper. P.S. acknowledges travel support from the International Programmes and Collaboration Division, BITS Pilani, India⁶. C.F. acknowledges funding provided by the Australian Research Council's Discovery Projects (grants DP150104329 and DP170100603), the ANU Futures Scheme, and the Australia-Germany Joint Research Cooperation Scheme (UA-DAAD). E. dC. gratefully acknowledges the Australian Research Council for funding support as the recipient of a Future Fellowship (FT150100079). S.D. is a Rutherford Fellow supported by the UK STFC. The authors also acknowledge the use of WebPlot Digitizer, an extremely useful online image-data mapping tool⁷.

This paper uses data from ALMA program ADS/JAO.ALMA #2011.0.00016.SV. ALMA is a partnership of ESO, NSF (USA), NINS (Japan), NRC (Canada), NSC and ASIAA (Taiwan), and KASI (Republic of Korea) and the Republic of Chile. The JAO is operated by ESO, AUI/NRAO and NAOJ.

REFERENCES

- ALMA Partnership et al., 2015, *ApJ*, **808**, L4
 Aceves H., Velázquez H., Cruz F., 2006, *MNRAS*, **373**, 632
 Battersby C., Bally J., Dunham M., Ginsburg A., Longmore S., Darling J., 2014, *ApJ*, **786**, 116
 Becerra F., Escala A., 2014, *ApJ*, **786**, 56
 Bertoldi F., McKee C. F., 1992, *ApJ*, **395**, 140
 Bigiel F., Leroy A., Walter F., Brinks E., de Blok W. J. G., Madore B., Thornley M. D., 2008, *AJ*, **136**, 2846
 Bigiel F., et al., 2011, *ApJ*, **730**, L13
 Blain A. W., Barnard V. E., Chapman S. C., 2003, *MNRAS*, **338**, 733
 Blanc G. A., Heiderman A., Gebhardt K., Evans II N. J., Adams J., 2009, *ApJ*, **704**, 842
 Bolatto A. D., Wolfire M., Leroy A. K., 2013, *ARA&A*, **51**, 207
 Bothwell M. S., et al., 2013, *MNRAS*, **429**, 3047
 Bouché N., et al., 2007, *ApJ*, **671**, 303
 Bournaud F., et al., 2014, *ApJ*, **780**, 57
 Bradač M., et al., 2017, *ApJ*, **836**, L2
 Braun H., Schmidt W., 2015, *MNRAS*, **454**, 1545
 Brisbin D., et al., 2017, *A&A*, **608**, A15
 Bussmann R. S., et al., 2013, *ApJ*, **779**, 25
 Cañameras R., et al., 2017, *A&A*, **604**, A117
 Caon N., Capaccioli M., D'Onofrio M., 1993, *MNRAS*, **265**, 1013
 Carilli C. L., Blain A. W., 2002, *ApJ*, **569**, 605
 Carilli C. L., Walter F., 2013, *ARA&A*, **51**, 105
 Casey C. M., 2012, *MNRAS*, **425**, 3094
 Chabrier G., 2003, *ApJ*, **586**, L133
 Chabrier G., Hennebelle P., Charlot S., 2014, *ApJ*, **796**, 75
 Chang Y.-Y., van der Wel A., da Cunha E., Rix H.-W., 2015, *ApJS*, **219**, 8
 Cibinel A., et al., 2017, *MNRAS*, **469**, 4683
 Ciotti L., Bertin G., 1999, *A&A*, **352**, 447
 Coppin K., et al., 2008, *MNRAS*, **384**, 1597
 Cowie L. L., Hu E. M., Songaila A., 1995, *AJ*, **110**, 1576
 Cresci G., et al., 2009, *ApJ*, **697**, 115
 Da Cunha E., Eminian C., Charlot S., Blaizot J., 2010a, *MNRAS*, **403**, 1894
 Da Cunha E., Charmandaris V., Díaz-Santos T., Armus L., Marshall J. A., Elbaz D., 2010b, *A&A*, **523**, A78
 Daddi E., et al., 2010, *ApJ*, **714**, L118
 Daddi E., et al., 2015, *A&A*, **577**, A46
 Danielson A. L. R., et al., 2017, *ApJ*, **840**, 78
 Decarli R., et al., 2016, *ApJ*, **833**, 70
 Downes D., Solomon P. M., 1998, *ApJ*, **507**, 615
 Draine B. T., Lee H. M., 1984, *ApJ*, **285**, 89
 Dunne L., Eales S., Edmunds M., Ivison R., Alexander P., Clements D. L., 2000, *MNRAS*, **315**, 115
 Dye S., et al., 2014, *MNRAS*, **440**, 2013
 Dye S., et al., 2015, *MNRAS*, **452**, 2258
 Elmegreen B. G., 2002, *ApJ*, **577**, 206
 Elmegreen B. G., 2015, *ApJ*, **814**, L30
 Elmegreen B. G., Hunter D. A., 2015, *ApJ*, **805**, 145
 Elmegreen B. G., Scalo J., 2004, *ARA&A*, **42**, 211
 Elmegreen D. M., Elmegreen B. G., Marcus M. T., Shahinyan K., Yau A., Petersen M., 2009, *ApJ*, **701**, 306
 Escala A., 2015, *ApJ*, **804**, 54
 Falgarone E., et al., 2017, *Nature*, **548**, 430
 Federrath C., 2013, *MNRAS*, **436**, 3167
 Federrath C., 2015, *MNRAS*, **450**, 4035
 Federrath C., Klessen R. S., 2012, *ApJ*, **761**, 156
 Federrath C., Klessen R. S., Schmidt W., 2008, *ApJ*, **688**, L79
 Federrath C., Roman-Duval J., Klessen R. S., Schmidt W., Mac Low M.-M., 2010, *A&A*, **512**, A81
 Federrath C., et al., 2016, *ApJ*, **832**, 143
 Förster Schreiber N. M., et al., 2009, *ApJ*, **706**, 1364
 Freundlich J., et al., 2013, *A&A*, **553**, A130
 Fudamoto Y., et al., 2017, *MNRAS*, **472**, 2028
 Gao Y., Solomon P. M., 2004, *ApJ*, **606**, 271
 Genzel R., et al., 2006, *Nature*, **442**, 786
 Genzel R., et al., 2010, *MNRAS*, **407**, 2091
 Griffin M. J., et al., 2010, *A&A*, **518**, L3
 Guo K., Zheng X. Z., Wang T., Fu H., 2015, *ApJ*, **808**, L49
 Gutermuth R. A., Pipher J. L., Megeath S. T., Myers P. C., Allen L. E., Allen T. S., 2011, *ApJ*, **739**, 84
 Hatsukade B., Tamura Y., Iono D., Matsuda Y., Hayashi M., Oguri M., 2015, *PASJ*, **67**, 93
 Hayward C. C., Kereš D., Jonsson P., Narayanan D., Cox T. J., Hernquist L., 2011, *ApJ*, **743**, 159

⁶ www.bits-pilani.ac.in/university/ipcd/home

⁷ <https://automeris.io/WebPlotDigitizer/index.html>

- Heiderman A., Evans II N. J., Allen L. E., Huard T., Heyer M., 2010, *ApJ*, **723**, 1019
- Hennebelle P., Chabrier G., 2011, *ApJ*, **743**, L29
- Hennebelle P., Chabrier G., 2013, *ApJ*, **770**, 150
- Hennebelle P., Falgarone E., 2012, *A&ARv*, **20**, 55
- Hezaveh Y. D., et al., 2013, *ApJ*, **767**, 132
- Hezaveh Y. D., et al., 2016, *ApJ*, **823**, 37
- Hildebrand R. H., 1983, *QJRAS*, **24**, 267
- Hodge J. A., Carilli C. L., Walter F., de Blok W. J. G., Riechers D., Daddi E., Lentati L., 2012, *ApJ*, **760**, 11
- Hodge J. A., et al., 2016, *ApJ*, **833**, 103
- Hogg D. W., Baldry I. K., Blanton M. R., Eisenstein D. J., 2002, *ArXiv Astrophysics e-prints*,
- Humason M. L., Mayall N. U., Sandage A. R., 1956, *AJ*, **61**, 97
- Ikarashi S., et al., 2015, *ApJ*, **810**, 133
- Immer K., Kauffmann J., Pillai T., Ginsburg A., Menten K. M., 2016, *A&A*, **595**, A94
- Inoue K. T., Minezaki T., Matsushita S., Chiba M., 2016, *MNRAS*, **457**, 2936
- Jameson K. E., et al., 2016, *ApJ*, **825**, 12
- Johnson S., Wilson G., Tang Y., AzTEC Team 2013, in *American Astronomical Society Meeting Abstracts #221*. p. 431.03
- Johnson T. L., et al., 2017, *ApJ*, **843**, L21
- Kauffmann J., Bertoldi F., Bourke T. L., Evans II N. J., Lee C. W., 2008, *A&A*, **487**, 993
- Kennicutt Jr. R. C., 1998a, *ARA&A*, **36**, 189
- Kennicutt Jr. R. C., 1998b, *ApJ*, **498**, 541
- Kennicutt R. C., Evans N. J., 2012, *ARA&A*, **50**, 531
- Khoperskov S. A., Vasiliev E. O., 2017, *MNRAS*, **468**, 920
- Klessen R. S., 2000, *ApJ*, **535**, 869
- Kovács A., Chapman S. C., Dowell C. D., Blain A. W., Ivison R. J., Smail I., Phillips T. G., 2006, *ApJ*, **650**, 592
- Kraljic K., Renaud F., Bournaud F., Combes F., Elmegreen B., Emsellem E., Teyssier R., 2014, *ApJ*, **784**, 112
- Krieger N., et al., 2017, *ApJ*, **850**, 77
- Krumholz M. R., McKee C. F., 2005, *ApJ*, **630**, 250
- Krumholz M. R., Dekel A., McKee C. F., 2012, *ApJ*, **745**, 69
- Krumholz M. R., Dekel A., McKee C. F., 2013, *ApJ*, **779**, 89
- Lada C. J., Lombardi M., Alves J. F., 2010, *ApJ*, **724**, 687
- Laporte N., et al., 2017, *ApJ*, **837**, L21
- Lehmann E., Casella G., 1998, *Theory of Point Estimation*. Springer Verlag
- Li A., Draine B. T., 2001, *ApJ*, **554**, 778
- Lu N., et al., 2015, *ApJ*, **802**, L11
- Lu N., et al., 2017, *ApJ*, **842**, L16
- Mac Low M.-M., Klessen R. S., 2004, *Reviews of Modern Physics*, **76**, 125
- Madau P., Dickinson M., 2014, *ARA&A*, **52**, 415
- Magdis G. E., et al., 2011, *ApJ*, **740**, L15
- Magdis G. E., et al., 2012, *ApJ*, **760**, 6
- McKee C. F., Ostriker E. C., 2007, *ARA&A*, **45**, 565
- McMullin J. P., Waters B., Schiebel D., Young W., Golap K., 2007, in *Shaw R. A., Hill F., Bell D. J., eds, Astronomical Society of the Pacific Conference Series Vol. 376, Astronomical Data Analysis Software and Systems XVI*. p. 127
- McNamara B. R., et al., 2014, *ApJ*, **785**, 44
- Miettinen O., Delvecchio I., Smolčić V., Aravena M., Brisbin D., Karim A., 2017, *A&A*, **602**, L9
- Molina F. Z., Glover S. C. O., Federrath C., Klessen R. S., 2012, *MNRAS*, **423**, 2680
- Narayanan D., Krumholz M. R., Ostriker E. C., Hernquist L., 2012, *MNRAS*, **421**, 3127
- Negrello M., et al., 2010, *Science*, **330**, 800
- Negrello M., et al., 2014, *MNRAS*, **440**, 1999
- Nguyen-Luong Q., et al., 2016, *ApJ*, **833**, 23
- Nightingale J. W., Dye S., 2015, *MNRAS*, **452**, 2940
- Ogilvie J., 1984, *Computers & Chemistry*, **8**, 205
- Oke J. B., Sandage A., 1968, *ApJ*, **154**, 21
- Onodera S., et al., 2010, *ApJ*, **722**, L127
- Ota K., et al., 2014, *ApJ*, **792**, 34
- Padoan P., Nordlund Å., 2011, *ApJ*, **730**, 40
- Papadopoulos P. P., van der Werf P. P., Xilouris E. M., Isaak K. G., Gao Y., Mühle S., 2012, *MNRAS*, **426**, 2601
- Paulino-Afonso A., et al., 2018, *MNRAS*,
- Pety J., et al., 2013, *ApJ*, **779**, 43
- Renaud F., Kraljic K., Bournaud F., 2012, *ApJ*, **760**, L16
- Rybak M., McKean J. P., Vegetti S., Andreani P., White S. D. M., 2015a, *MNRAS*, **451**, L40
- Rybak M., Vegetti S., McKean J. P., Andreani P., White S. D. M., 2015b, *MNRAS*, **453**, L26
- Salim D. M., Federrath C., Kewley L. J., 2015, *ApJ*, **806**, L36
- Salpeter E. E., 1955, *ApJ*, **121**, 161
- Sargent M. T., et al., 2014, *ApJ*, **793**, 19
- Schmidt M., 1959, *ApJ*, **129**, 243
- Schreiber C., et al., 2015, *A&A*, **575**, A74
- Scoville N., et al., 2017, *ApJ*, **836**, 66
- Sersic J. L., 1968, *Atlas de Galaxias Australes*
- Shapiro K. L., Genzel R., Förster Schreiber N. M., 2010, *MNRAS*, **403**, L36
- Shi Y., Helou G., Yan L., Armus L., Wu Y., Papovich C., Stierwalt S., 2011, *ApJ*, **733**, 87
- Silk J., 1997, *ApJ*, **481**, 703
- Simpson J. M., et al., 2015, *ApJ*, **799**, 81
- Smail I., Ivison R. J., Blain A. W., 1997, *ApJ*, **490**, L5
- Smail I., Ivison R. J., Blain A. W., Kneib J.-P., 2002, *MNRAS*, **331**, 495
- Smith D. J. B., et al., 2013, *MNRAS*, **436**, 2435
- Solomon P. M., Vanden Bout P. A., 2005, *ARA&A*, **43**, 677
- Solomon P. M., Radford S. J. E., Downes D., 1992a, *Nature*, **356**, 318
- Solomon P. M., Downes D., Radford S. J. E., 1992b, *ApJ*, **398**, L29
- Speagle J. S., Steinhardt C. L., Capak P. L., Silverman J. D., 2014, *ApJS*, **214**, 15
- Spilker J. S., et al., 2016, *ApJ*, **826**, 112
- Springel V., Hernquist L., 2003, *MNRAS*, **339**, 312
- Swinbank A. M., et al., 2015, *ApJ*, **806**, 5
- Tacconi L. J., et al., 2008, *ApJ*, **680**, 246
- Tacconi L. J., et al., 2010, *Nature*, **463**, 781
- Tamura Y., Oguri M., Iono D., Hatsukade B., Matsuda Y., Hayashi M., 2015, *PASJ*, **67**, 72
- Trujillo I., Graham A. W., Caon N., 2001, *MNRAS*, **326**, 869
- Valtchanov I., et al., 2011, *MNRAS*, **415**, 3473
- Van den Bergh S., Abraham R. G., Ellis R. S., Tanvir N. R., Santiago B. X., Glazebrook K. G., 1996, *AJ*, **112**, 359
- Warren S. J., Dye S., 2003, *ApJ*, **590**, 673
- Wong T., Blitz L., 2002, *ApJ*, **569**, 157
- Wong K. C., Suyu S. H., Matsushita S., 2015, *ApJ*, **811**, 115
- Wong K. C., Ishida T., Tamura Y., Suyu S. H. and Oguri M., Matsushita S., 2017, *ApJ*, **843**, L35
- Wright E. L., 2006, *PASP*, **118**, 1711
- Wu J., Evans II N. J., Gao Y., Solomon P. M., Shirley Y. L., Vanden Bout P. A., 2005, *ApJ*, **635**, L173
- Wu J., Evans II N. J., Shirley Y. L., Knez C., 2010, *ApJS*, **188**, 313
- Xu C. K., et al., 2015, *ApJ*, **799**, 11
- Yang C., et al., 2017, *A&A*, **608**, A144
- Zanella A., et al., 2015, *Nature*, **521**, 54